

Transition to chaotic scattering

Mingzhou Ding*

*Laboratory for Plasma Research and Department of Physics,
University of Maryland, College Park, Maryland 20742*

Celso Grebogi

*Laboratory for Plasma Research, Department of Mathematics, and Institute for Physical Science and Technology,
University of Maryland, College Park, Maryland 20742*

Edward Ott

*Laboratory for Plasma Research, Department of Physics, and Department of Electrical Engineering,
University of Maryland, College Park, Maryland 20742*

James A. Yorke

*Institute for Physical Science and Technology and Department of Mathematics,
University of Maryland, College Park, Maryland 20742*

(Received 17 May 1990)

This paper addresses the question of how chaotic scattering arises and evolves as a system parameter is continuously varied starting from a value for which the scattering is regular (i.e., not chaotic). Our results show that the transition from regular to chaotic scattering can occur via a saddle-center bifurcation, with further qualitative changes in the chaotic set resulting from a sequence of homoclinic and heteroclinic intersections. We also show that a state of “fully developed” chaotic scattering can be reached in our system through a process analogous to the formation of a Smale horseshoe. By fully developed chaotic scattering, we mean that the chaotic-invariant set is hyperbolic, and we find for our problem that *all* bounded orbits can be coded by a full shift on three symbols. Observable consequences related to qualitative changes in the chaotic set are also discussed.

I. INTRODUCTION

Chaotic scattering occurs in a variety of situations of practical interest, including satellite encounters in celestial mechanics,¹ molecular dynamics,² vortex pair scattering in fluid dynamics,³ and classical potential scattering of point particles.^{4–6} In this paper we consider scattering from potentials which depend on some set of parameters. For example, if the physical space is two dimensional and the potential consists of a number of hills, then the parameters might be such as to characterize the heights of the individual hills and the relative locations of the centers of the hills. Given such a situation it is natural to ask how chaotic scattering arises and evolves when these system parameters are allowed to vary. That is, given a set of parameters where the scattering is regular (i.e., not chaotic), what are the typical sequences of events (“routes”) that occur as parameters are varied and the scattering becomes chaotic? This is the question addressed in the present paper.

Most of the previous work on chaotic scattering has concerned systems with fixed potential parameters and fixed scattering particle energy. This past research has clarified the phenomenology of chaotic scattering, the structure of the fractal invariant sets responsible for the observed chaos, and the role of unstable periodic orbits in determining the scattering process. In particular, some of these results are the following. Initial conditions on a

set of Lebesgue measure zero in the phase space lead to orbits that are trapped in the scattering region for an arbitrarily long time. This is because of the existence of unstable invariant sets in the potential region. The trapping initial conditions lie on the stable manifolds of these invariant sets. If the scattering is regular, the invariant set can be very simple, e.g., a few isolated periodic orbits and their associated stable and unstable manifolds. For chaotic scattering the invariant set is complicated, involving Cantor-set-type structure on all scales. Due to the presence of such chaotic sets, the scattering process exhibits two prominent features. First, a particle trajectory can be very complicated in the potential region, even though it only spends a finite amount of time in the region before it heads off to infinity. Second, if we plot the dependence of some variable characterizing the outgoing trajectory against some other variable characterizing the initial condition, then this function can be very complicated, displaying extreme sensitivity of the outgoing variable to changes in the initial condition. Specifically, the function is singular (“infinitely sensitive”) on a Cantor set of initial condition values. Furthermore, this Cantor set in the initial conditions is just those initial conditions that lie on the stable manifold of the chaotic-invariant set.

Recently, some progress has been made on the general problem we address in this paper: understanding how and why scattering can become chaotic as a parameter is varied.^{5,6} In Ref. 6 the authors argue that the onset of

chaotic scattering can be achieved either through a saddle-center bifurcation or through another, new type of bifurcation which they call an abrupt bifurcation and that, for two degrees of freedom systems, these are the only two generic routes to chaotic scattering. They performed detailed analysis of the abrupt bifurcation but did not investigate the consequences of the saddle-center bifurcation route to chaotic scattering. In this paper we study the saddle-center bifurcation route by investigating a particular model scattering problem and use the results so obtained to draw some general conclusions.

We show how the onset of chaotic scattering can be obtained via a saddle-center bifurcation, and we demonstrate how the character of the chaotic scattering process changes as the parameter is varied. Starting from a stage where the scattering is regular, we observe that the saddle-center bifurcation marks the transition from regular to chaotic scattering. Immediately after this bifurcation, the stable and unstable manifolds of the newborn saddle intersect each other and a chaotic set is therefore generated. The next important state in the evolution of chaotic scattering in our model is the occurrence of a heteroclinic tangency between the stable and unstable manifolds of the saddle which came into existence at the saddle-center bifurcation and the stable and unstable manifolds of another saddle which exists throughout the course of the system evolution. This event not only causes qualitative changes in the chaotic set, but it also marks the beginning of the formation of a structure topologically equivalent to a horseshoe-type map. As the parameter changes further, the chaotic scattering set becomes hyperbolic [in particular, in the hyperbolic parameter range, there are no Kolmogorov-Arnold-Moser (KAM) surfaces, no stable periodic orbits, and the dynamics is described by a full shift on three symbols]. This is in contrast with the “abrupt bifurcation,” studied in Ref. 6, for which the scattering set changes from non-chaotic directly to hyperbolic chaotic as a parameter passes through a critical value. The fact that the dynamics in our model is hyperbolic in some range of the parameter is significant because it implies that no bifurcations annihilating or creating periodic orbits can occur (e.g., there are no saddle-center or period-doubling bifurcations in the hyperbolic range). Such a hyperbolic situation has been called⁶ “fully developed chaotic scattering.” One of the important results obtained from observing this sequence of events is that stable-unstable manifold intersections not only lead to sudden changes in the chaotic-invariant set, but also have clearly observable global effects on the behavior of the scattering properties of the potential.

The potential we use to perform our analysis is illustrated in Fig. 1. It consists of three nonoverlapping potential hills with their centers on the vertices of an isosceles triangle. Each individual hill is circularly symmetric and can be represented as

$$\Phi_i(x,y) = V_i \left\{ 1 - \left[\frac{(x-x_i)^2 + (y-y_i)^2}{a_i^2} \right] \right\} \quad (1)$$

for $(x-x_i)^2 + (y-y_i)^2 \leq a_i^2$,

and $\Phi_i(x,y) = 0$ for $(x-x_i)^2 + (y-y_i)^2 > a_i^2$. In Eq. (1),

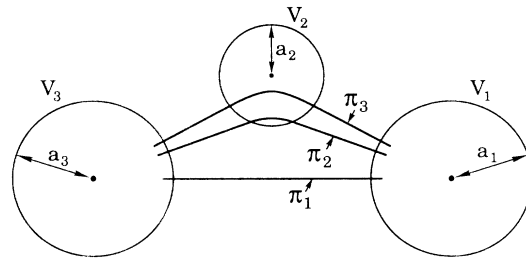


FIG. 1. Top view of the three potential hills defined by Eqs. (1) and (2) and the three periodic orbits π_1 , π_2 , and π_3 . π_2 and π_3 are created at the saddle-center bifurcation.

$i = 1, 2, 3$, (x_i, y_i) is the center of the i th potential hill, a_i is the hill radius, and V_i is the hill height. The coordinate system is such that the vertical line through the center of hill 2 is the y axis, the horizontal line through the centers of hills 1 and 3 is the x axis, and their intersection is the origin. The full potential is then symmetric with respect to the y axis and can be written as

$$\Phi(x,y) = \Phi_1(x,y) + \Phi_2(x,y) + \Phi_3(x,y). \quad (2)$$

Since each potential hill is a paraboloid of revolution, the equation of motion can be solved exactly inside each of the regions $(x-x_i)^2 + (y-y_i)^2 \leq a_i^2$, and there is no need for numerical integration of differential equations. For a particle traveling outside the hill regions, the trajectory is a straight line. As compared to more general $\Phi(x,y)$, this both saves computer time and improves the accuracy of our calculations. Throughout most of this paper we fix the geometrical configuration of the potential (i.e., x_i , y_i , and a_i), the particle energy E_p , the potential heights $V_1 = V_3 \gg E_p$, and then investigate the system behavior as a function of the control parameter V_2 .

As we have already mentioned, we find that as the parameter V_2 is varied, we come to a range of V_2 where the chaotic-invariant set is hyperbolic. To understand the nature of this hyperbolic set refer to Fig. 1. The solid lines labeled by π_1 , π_2 , and π_3 in Fig. 1 are trajectories of three different unstable periodic orbits which travel back and forth between hills 1 and 3. We find that all bounded orbits are made up of sequences of “legs” bouncing between hills 1 and 3 in the three possible ways illustrated. That is, each leg of a bounded orbit passes close to π_1 , π_2 , or π_3 and can be uniquely associated with that unstable periodic orbit. We emphasize that all sequences of legs are possible and that no bounded orbits other than these are permissible. Thus the chaos, in this parameter range of V_2 , is completely described by a full shift of three symbols.

One of the notable aspects of the situation just described is that the orbit deflection provided by hill 2 results in two (rather than only one) possible paths between hills 1 and 3: one path which penetrates close to the potential peak of hill 2 (resulting in π_3), and one which stays further away from this peak (resulting in π_2). An interesting question (to be discussed in Sec. III C) concerns what happens to our picture of the full three shift chaos as the height of hill 2 increases through E_p (i.e., V_2

becomes greater than the particle energy). In this case, one can regard the single periodic orbit π_3 as bifurcating into two periodic orbits: one bouncing between hills 1 and 2 and the other between hills 3 and 2. For hills of small enough radii compared to their separations, we find that a new type of bifurcation which massively changes the hyperbolic chaotic set takes place at $V_2 = E_p$. In particular, in this bifurcation the infinite number of bounded orbits whose sequences of legs contained segments coded by π_3 are destroyed and a new class of bounded orbits is created. For this new class of orbits we can again construct a symbolic dynamics which is a full three shift.

The organization of this paper is as follows. In Sec. II we introduce our numerical techniques and discuss regular scattering and its characterization. In Sec. III we present our results on the saddle-center bifurcation and the subsequent homoclinic and heteroclinic intersections. We emphasize the existence of a horseshoe-type map describing the dynamics of the system and the massive bifurcation at $V_2 = E_p$. In the same section we discuss observable consequences of the major qualitative changes that we find in the invariant set. In Sec. IV we summarize our results and conclusions.

II. NUMERICAL EXPERIMENTS AND REGULAR SCATTERING

In this section we discuss the simple system obtained by letting $V_2 = 0$ in Fig. 1 and in Eq. (1). A major reason for doing this is to simply introduce and illustrate the numerical techniques we will be using later. Because of the simplicity of this case (two identical hills), the scattering is regular and all aspects of the scattering process can be understood. Since the height of the hills is presumed larger than the energy of scattering particles, there is a periodic orbit π_1 which bounces back and forth between the two hills along the line joining their centers (Fig. 1). The orbit π_1 and its stable and unstable manifolds are the only invariant sets in this case.

For definiteness, we choose $x_1 = -x_3 = 6$, $y_1 = y_3 = 0$, $a_1 = a_3 = 3$, $V_1 = V_3 = 10$, and $E_p = 1$ [cf. Eq. (1)]. Furthermore, we choose initial conditions lying on the line $y = 6$, with the additional assumption that the initial particle velocity is straight down (parallel to the y axis). Thus such initial conditions will be specified by x_0 the x coordinates of particles on that line. The parameter x_0 is also referred to as the impact parameter in the scattering theory. Some of the initial conditions give rise to trajectories that are simply downward-going straight lines that never hit either of the potential hills. Other initial conditions correspond to orbits which hit the hills and bounce between them a number of times before heading off (along straight line paths) to infinity. Due to the symmetry present in the potential, we need only consider initial conditions with positive x coordinates ($x_0 > 0$). Figure 2 displays the trajectories of a few particles with different impact parameters. Note that the range of impact parameters used in Fig. 2 is very narrow so that, to the resolution of the figure, the down-going initial legs of the trajectories appear to be the same for all the particles. After bouncing in the potential, however, various trajectories

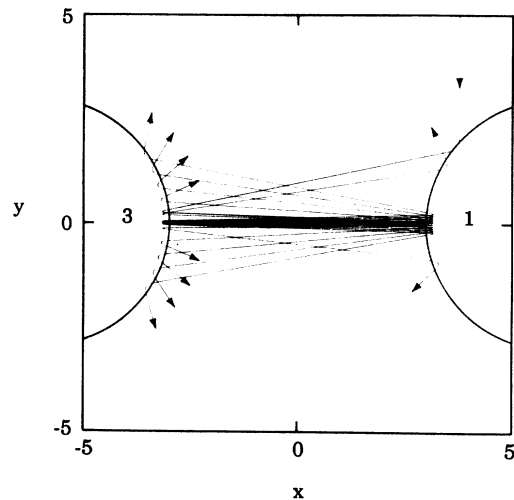


FIG. 2. Trajectories of ten particles with initial conditions x_0 ranging from 3.7564 to 3.7566.

separate as shown.

In our first numerical experiment we uniformly space a large number of particles, say 10000, over an interval of impact parameters, let these particles descend toward the potential region, and follow their orbits until they exit the region of the potential, never to return. We then plot the angle θ between the outgoing particle velocity and the y axis as a function of the impact parameter x_0 [Fig. 4(a)]. Here the definition of θ is shown in Fig. 3, and θ is taken to lie in the range $[-\pi, \pi]$. We also obtain plots of “exit time” versus impact parameter [Fig. 4(b)]. By “exit time” we mean the amount of time a particle spends from the time it first hits a hill [i.e., when it first satisfies $(x - x_i)^2 + (y - y_i)^2 = a_i^2$ for some i] to the time it last leaves a hill [i.e., when it last satisfies $(x - x_i)^2 + (y - y_i)^2 = a_i^2$ for some i], after which it heads off to infinity. We observe a sharp peak in the exit time plot Fig. 4(b). If we increase our resolution near this peak as shown in the enlargement, Fig. 4(d), we see that the peak gets higher and higher. This indicates that there is an impact parameter value near the finite resolution peak in the plot for which the exit time is infinite. This point is indicated by the arrows on the x_0 axis of Figs. 4. Another interesting observation is that the location of

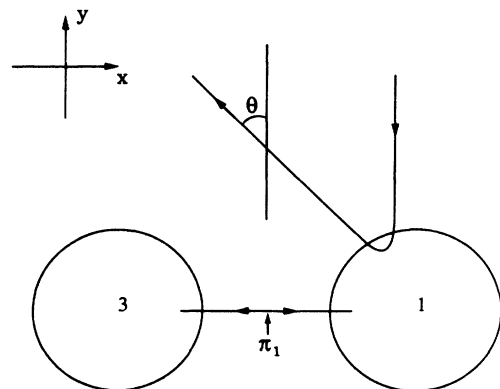


FIG. 3. A particle trajectory and the definition of the exit angle θ .

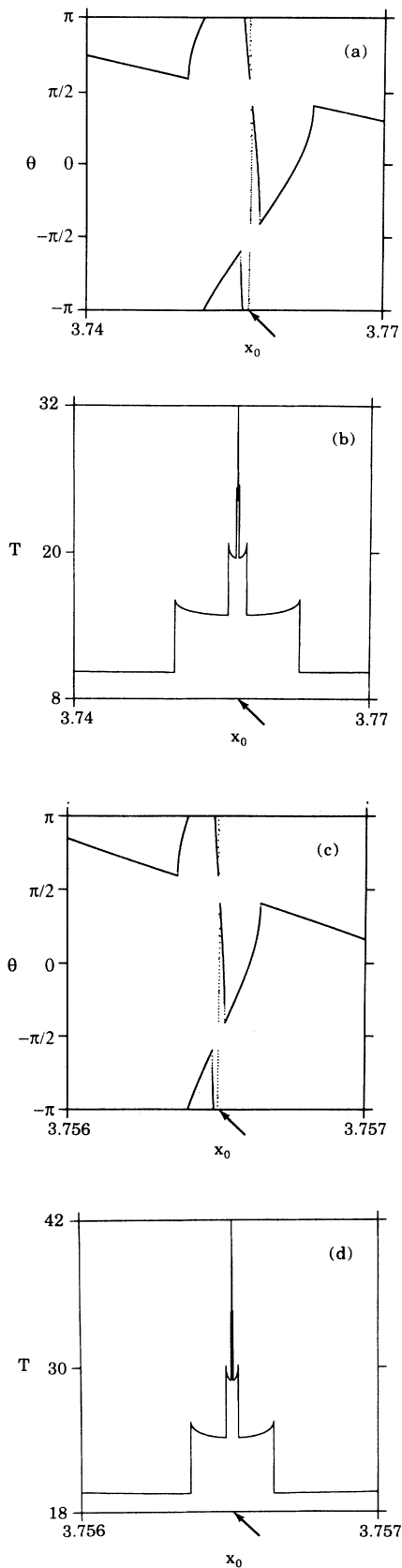


FIG. 4. (a) and (c) exit angle vs the impact parameter; (b) and (d) exit time vs the impact parameter; (c) and (d) enlargements of (a) and (b), respectively ($V_2=0$).

this peak also serves to separate the initial conditions of particles exiting upward ($|\theta| < \pi/2$) and downward ($|\theta| > \pi/2$). [As can be seen in Fig. 4(a) and its enlargement Fig. 4(c), $|\theta|$ is always less than $\pi/2$ to the right of the arrow on the x_0 axis and is always greater than $\pi/2$ to the left.]

The value of x_0 where the exit time is infinite corresponds to the place where the stable manifold of the periodic orbit π_1 intersects the line of initial conditions $y=6$. To illustrate this we send a number of particles to the potential region with initial conditions straddling the value indicated by the arrow on x_0 axis in Fig. 4. The trajectories of these particles are the ones shown in Fig. 2. They first approach the periodic orbit and then stay close to it for a while before leaving the potential region. The closer an initial condition is to the stable manifold, the longer it stays close to the periodic orbit, and the longer it takes to exit the potential. Another thing which we note from Fig. 2 and Figs. 4(a) and 4(c) is that at the stable manifold point, θ is infinitely sensitive to x_0 . That is, arbitrarily small changes in x_0 sufficiently near this stable manifold point make large changes in θ . In what follows we often refer to the plots in Figs. 4 as scattering functions.

In the second numerical experiment we again send a large number of particles, say 30 000, with impact parameters uniformly spaced in some interval, say $3.75 < x_0 < 3.76$, of the line $y=6$ into the potential region, and examine the "particle decay process" by plotting the number of particles $N(T)$ which, after a time T , are still left in the region (i.e., have not yet experienced their last encounter with one of the potential hills) as a function of T . This is shown in Fig. 5(a). Figure 5(b) displays a semilogarithmic plot of the same data shown in Fig. 5(a). The result is a straight line (shown dashed) with periodic oscillations. It can be seen from numerical and theoretical evidence that $N(T)$ scales approximately with T as

$$N(T) \sim e^{-\mu T}. \quad (3)$$

The slope of the dashed line in Fig. 5(b) gives μ , which is also

$$\mu = \ln(\lambda_p) / T_p \quad (4)$$

where λ_p and T_p are defined in the figure. The origin of the exponent μ can be understood in terms of the period and eigenvalues of the orbit π_1 (see Appendix A).

We now introduce another numerical technique which is used throughout our study, namely, the Poincaré surface of section. For a time-independent Hamiltonian system, the energy is an integral of the motion and (for systems of two degrees of freedom) the motion in the four-dimensional phase space is restricted to the three-dimensional energy surface. Hence a surface of section transversal to the particle trajectory yields a two-dimensional area-preserving map. For the present system we place our surface of section at $x=0$. As coordinates on the surface of section ($x=0$), we use the y coordinate and the y component of the velocity v_y ($\mathbf{p}=\mathbf{v}$ for particles with unit mass). For a given point (v_y, y) on the surface

of section there are two possible points on the energy surface with opposite signs of v_x which it could correspond with, $(v_y, y, v_x, 0)$ and $(v_y, y, -v_x, 0)$. In such a case, the usual way of eliminating the ambiguity between the two possible choices is to only count a point to be on the surface of section if the orbit crosses the surface in a particular direction (e.g., from $x < 0$ to $x > 0$, implying $v_x > 0$). In our case this is not necessary. In particular, we note that the system in Fig. 1 possesses a reflection symmetry about $x=0$. Thus both of the points, $(v_y, y, v_x, 0)$ and $(v_y, y, -v_x, 0)$, when evolved forward in time, yield orbits which next intersect the surface of section at the same point (i.e., with the same v_y and y coordinate values). This allows us to identify crossings coming from either side of the $x=0$ plane as equivalent and thus we can accumulate twice as many points on the surface of section for an orbit of a given length. We denote the resulting discrete Poincaré map as P . Then, $(v_y', y') = P(v_y, y)$, where (v_y', y') denotes the next surface of section crossing following the one at (v_y, y) . Note that for some points on the surface of section the image under P may not exist, because the corresponding trajectories can leave the surface of section without ever returning to it. (For those points P is undefined.)

On the surface of section the periodic orbit π_1 is represented by a single fixed point which for the potential being considered here is the origin, $(v_y, y) = (0, 0)$. The eigenvalues of P numerically evaluated at this point for

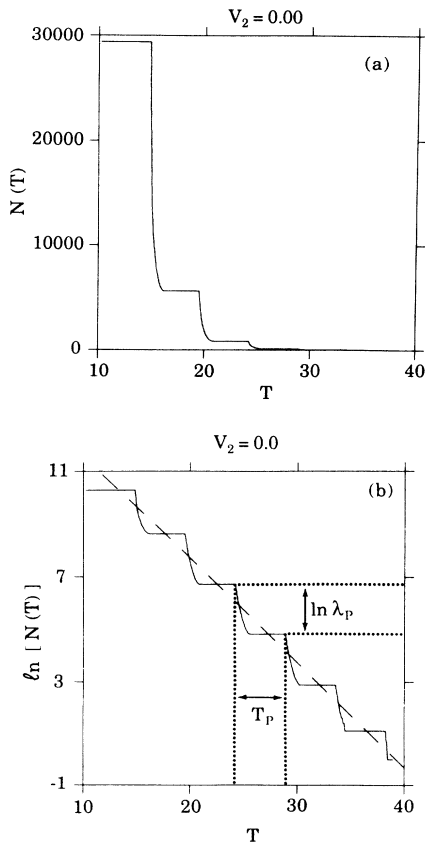


FIG. 5. (a) Plot of $N(T)$ vs T and (b) semilogarithmic plot of the same data in (a).

the system configuration specified in this section are $\lambda_1 \approx 6.7$ and $\lambda_2 = 1/\lambda_1$. Knowing the location of the fixed point, one can numerically determine its stable and unstable manifolds by making use of the sprinkler method:⁷ take a small square on the surface of section containing the fixed point, uniformly sprinkle a large number of points in the square, say, 10^6 , let these points evolve under P for a certain number of iterations, and plot the points which are still left on the section. These points give us the approximate location of the intersection of the unstable manifold with the surface of section. To obtain the stable manifold we first note the basic time reversal symmetry of the dynamics implied by the invariance of the Hamiltonian to the transformation $\mathbf{v} \rightarrow -\mathbf{v}$. This implies that each point on the unstable manifold (v_u, x_u) corresponds to a point on the stable manifold $(v_s, x_s) = (-v_u, x_u)$ and vice versa. To obtain the intersection of the stable manifold with the surface of the section we further note the equivalence of points in the surface of section with the same $|v_x|$ but opposite signs of v_x . Thus to each unstable manifold point (v_{yu}, y_u) in the surface of section there corresponds a stable manifold point $(v_{ys}, y_s) = (-v_{yu}, y_u)$. That is, the intersection of the stable manifold with the surface of section can be obtained from the intersection of the unstable manifold with the surface of section by reflecting the unstable manifold intersection through the y axis. Figure 6 shows the computed manifolds, and they appear (as they should) to be straight lines.

Now we are in a position to perform our third numerical experiment, in which we take a small interval of initial conditions on the line $y=6$ such that this interval contains the intersection of the stable manifold with the $y=6$ line. We then place 2000 uniformly spaced initial conditions in this interval and evolve them under the equations of motion. Then we take the resulting first orbit crossing with the surface of section. This gives an image I of the crossing of the original interval with the surface of section. In Fig. 7 we superpose I on the data of Fig. 6. As we should expect, the interval I intersects the stable manifold transversely. In addition, upon further application of P , the points of I falling in the upper middle section of Fig. 7 follow the stable manifold downward

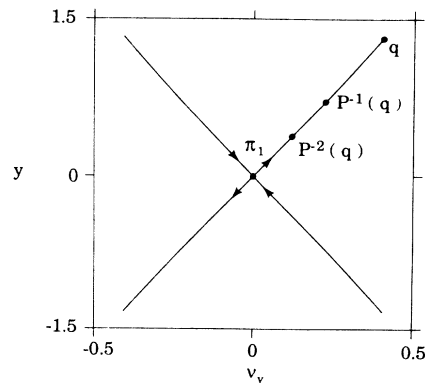


FIG. 6. The intersection of the stable and unstable manifolds of π_1 with the surface of section $x=0$ ($V_2=0$).

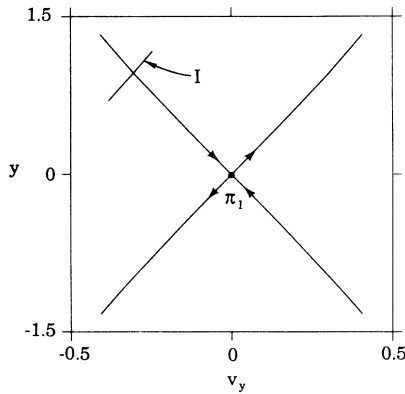


FIG. 7. The image I of the interval of initial conditions $3.74 < x_0 < 3.77$ on the surface of section $x=0$ superposed on the data shown in Fig. 6 ($V_2=0$).

first and then follow the upward branch of the unstable manifold and exit upward; in contrast, those falling in the left section of Fig. 7 map downward and exit downward following the downward branch of the unstable manifold.

Before concluding this section, we remark that the addition of a sufficiently small middle hill (hill 2) to the two-hill system does not alter the essential character of the scattering process. This has been verified numerically and also follows from the hyperbolicity of the periodic orbit π_1 . Nevertheless, some changes in both the surface of section and the scattering functions do take place. Most noticeable among them is the appearance of ripples in the stable and unstable manifolds on the surface of section caused by the presence of the sharp edge of the middle hill at $(x-x_2)^2 + (y-y_2)^2 = a_2^2$. An important effect of these ripples can be seen with reference to Fig. 7. In particular, the image of the initial condition interval can intersect the stable manifold of π_1 at more than one point (e.g., three points). Each such intersection corresponds to a singularity of the scattering function.

III. CHAOS INDUCED BY HOMOCLINIC AND HETEROCLINIC INTERSECTIONS

In this section we discuss qualitative changes in the scattering behavior as the control parameter V_2 (the height of the middle hill) is increased. To perform our numerical experiments we choose the following set of parameters for the potential and for the scattering particle: $x_1 = -x_3 = 6$, $y_1 = y_3 = 0$, $x_2 = 0$, $y_2 = 2.2$; $a_1 = a_3 = 3$, $a_2 = 2$; $V_1 = V_3 = 10$, $V_2 > 0$, and $E_p = 1$.

A. Saddle-center bifurcation and the onset of chaos

The first significant event that occurs, as the parameter V_2 is increased, is a saddle-center bifurcation at $V_2 = V_{sc}$ ($V_{sc} \approx 0.187$). This bifurcation results in the creation of a pair of periodic orbits traveling between hills 1 and 3 through hill 2. Figures 8 illustrate the system evolution around this saddle-center bifurcation in the physical space. For $V_2 < V_{sc}$, the system has only one periodic orbit π_1 and the scattering is regular [Fig. 8(a)]. As V_2 passes through V_{sc} , the saddle and the center, which ini-

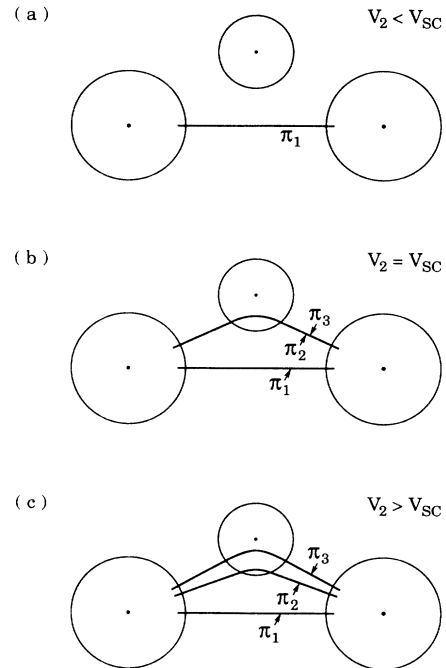


FIG. 8. (a) The only periodic orbit π_1 for $V_2 < V_{sc}$; (b) the newborn saddle π_3 and center π_2 coincide with each other at $V_2 = V_{sc}$; (c) π_2 and π_3 move apart from each other for $V_2 > V_{sc}$.

tially coincide when they are created at V_{sc} , move apart from each other [Figs. 8(b) and 8(c)]. The upper orbit in Fig. 8(c), which we henceforth denote as π_3 , is a regular saddle (both eigenvalues of the Poincaré surface of section map are real and positive); while the middle orbit in Fig. 8(c) (denoted by π_2) is a center (both eigenvalues are complex and lie on the unit circle in the complex plane). As soon as the saddle and center move apart, in generic situations, the saddle π_3 will immediately have its stable and unstable manifolds intersect each other transversely.⁸ According to Smale's theory, such homoclinic intersections imply the existence of chaotic-invariant set. Therefore the saddle-center bifurcation signifies the onset of chaotic scattering. Figures 9 illustrate schematically the corresponding evolution pattern on the surface of section around $V_2 = V_{sc}$. Figure 9(a) shows the unstable periodic orbit π_1 and its stable and unstable manifolds for $V_2 < V_{sc}$. Figure 9(b) shows the newborn saddle-center at $V_2 = V_{sc}$ together with its invariant manifolds. Figure 9(c) displays the saddle π_3 and the center π_2 after they move apart from each other and the homoclinic tangle formed by the stable and unstable manifolds of π_3 . Notice that surrounding the center π_2 is an "island region" consisting of a nested family of KAM tori between which are periodic orbits, chaotic components, and higher-order island chains. The numerically computed island accompanying the center π_2 for $V_2 = 0.195$ is shown in Fig. 10. Such islands in Hamiltonian dynamics can exert strong influence on the particle decay process (cf. the second numerical experiment described in Sec. II).⁹ As we increase V_2 further, the center π_2 undergoes a period-doubling bi-

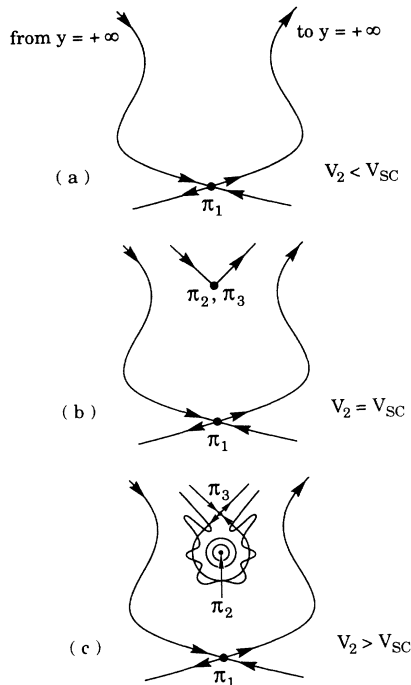


FIG. 9. (a) π_1 and its invariant manifolds for $V_2 < V_{sc}$; (b) the newborn saddle center at $V_2 = V_{sc}$; (c) homoclinic intersections between the stable and unstable manifolds of π_3 occur for $V_2 > V_{sc}$.

furcation and becomes an unstable saddle (both eigenvalues of the Poincaré map are real and negative; such an orbit is sometimes called a twisted saddle). Figure 11 shows the new centers (period two) and their surrounding island structure just after the period-doubling bifurcation at $V_2 \approx 0.207$. Numerical evidence indicates that the period-doubling process continues *ad infinitum*. The existence of such an infinite cascade of period doubling in our system is in agreement with a theory developed in Ref. 10 concerning the origin of the occurrence of an infinite number of periodic orbits in a chaotic set.

The appearance of the chaotic set after the saddle-center bifurcation has strong impact on the observable

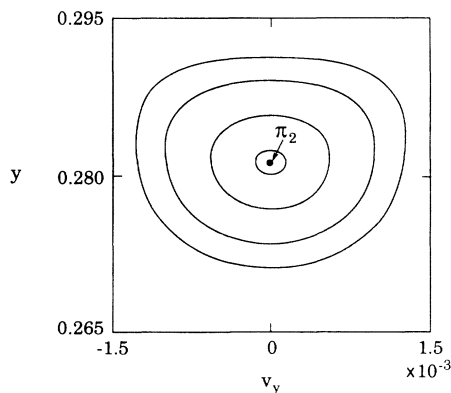


FIG. 10. The island structure associated with the center π_2 ($V_2 = 0.195$).

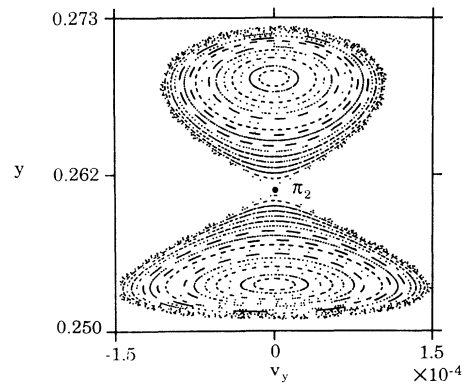


FIG. 11. The new center of period two and its associated island structure after π_2 underwent period-doubling bifurcation ($V_2 = 0.207$).

behavior of the system. Figures 12 show the scattering function for the value of $V_2 = 0.195$ [corresponding to the situation shown in Fig. 9(c)]. As we have already discussed in Sec. II, the peaks observed in the exit time plots are the intersections of the stable manifolds of the invariant set with the line of initial conditions $y = 6$. The main difference between this case where the invariant set is chaotic and the case in Sec. II where the invariant set is nonchaotic is that now the peaks apparently reside on a Cantor set. Thus if we blow up a region about one of these peaks we see more peaks and their heights increase [compare Figs. 12(b) and 12(d)]. Another interesting thing to note is that chaos can only be experienced by particles exiting upward, i.e., $|\theta| < \pi/2$, as shown in Figs. 12(a) and 12(c). The scattering function for downward exiting particles is still regular and governed essentially by the original saddle π_1 and its stable and unstable manifolds. The reason why this is so can be understood in the following way. Consider particles that experience chaotic scattering, their first images on the surface of section lie in the region where the intersection of the stable and unstable manifolds of π_3 occurs (cf. the third experiment described in Sec. II). As can be seen in Fig. 9(c), this region is completely contained between the branch of the unstable manifold of π_1 that extends from π_1 to $y = +\infty$ and the branch of the stable manifold of π_1 that also extends from π_1 to $y = +\infty$. Note that these branches of the stable and unstable manifolds form barriers which the points on the surface of section cannot cross. In other words, the region enclosed between the two branches of the invariant manifolds of π_1 is invariant under the scattering dynamics. Thus those particles that experience chaotic scattering must follow the upward branch of the unstable manifold of π_1 to exit the potential region ($|\theta| < \pi/2$). On the other hand, if a particle exits downward ($|\theta| > \pi/2$), its first image on the surface of section must land on the other side of the stable manifold of π_1 where no chaotic set is present.

B. Heteroclinic intersections and fully developed chaotic scattering

As we continue to increase V_2 the two periodic orbits created at the saddle-center bifurcation move further

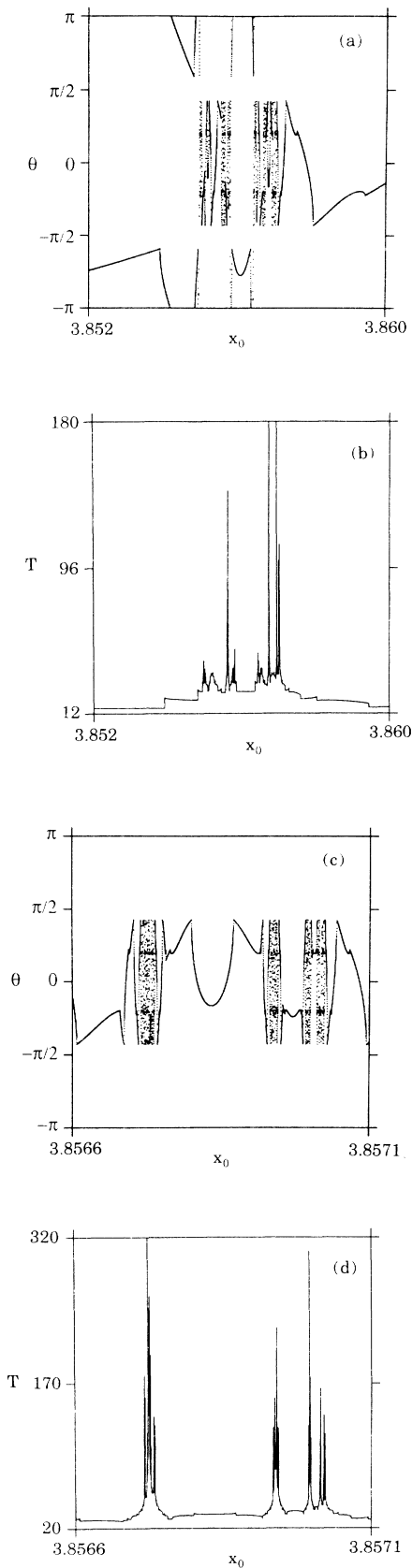


FIG. 12. (a) and (c) exit angle vs the impact parameter; (b) and (d) exit time vs the impact parameter; (c) and (d) enlargements of (a) and (b), respectively ($V_2 = 0.195$).

apart from one another. The stable and unstable manifolds of the saddle π_3 pull away from each other along the v_y direction. Meanwhile, the stable and unstable manifolds of the original saddle π_1 squeeze in toward each other along the v_y direction. This motion leads the two sets of manifolds to form a heteroclinic tangency at $V_2 = V_{h1}$ ($V_{h1} \approx 0.215$). A schematic illustration of the situation is given in Fig. 13. If V_2 is increased slightly past V_{h1} , then the stable and unstable manifolds of the two saddles cross each other, giving rise to heteroclinic intersections. The chaotic set, which used to involve the manifolds of the saddle π_3 only, suddenly enlarges to include the stable and unstable manifolds of the original saddle π_1 . Figures 14 show the scattering functions for $V_2 = 0.25 > V_{h1}$, and Fig. 15 shows the numerically computed heteroclinic tangle for the same parameter value on the surface of section. Note from Figs. 14 that, corresponding to the fact that the chaos is no longer restricted to the region between the upward branches of the invariant manifolds of π_1 , there is now chaotic motion for particles exiting both upward and downward. This is in contrast with the case $V_2 < V_{h1}$ (cf. Figs. 12). Thus the occurrence of the heteroclinic tangency results in a clearly observable sudden qualitative change in the character of the θ versus x_0 plot.

As we increase V_2 further, the stable and unstable manifolds of π_3 continue their relative motion in the v_y direction, while the upward branches of the stable and unstable manifolds of π_1 continue to move towards each other. Eventually, we come to the situation shown in Fig. 16. For the potential specified at the beginning of this section, we find numerically that Fig. 16 applies for V_2 in the range $V_- < V_2 < V_+ < E_p$, where $V_- \approx 0.265$ and $V_+ \approx 0.275$. Figures 17 pictorially illustrate the sets of stable and unstable manifolds of the two regular saddles π_1 and π_3 for five cases: $V_2 = V_{h1}$, $V_{h1} < V_2 < V_-$, $V_2 = V_-$, $V_- < V_2 < V_+$, and $V_2 = V_+$.

Examining the situation in the middle of the interval $V_- < V_2 < V_+$ we see no evidence of stable periodic orbits or KAM surfaces, and we observe that none of the stable-unstable manifold intersections which we calculate

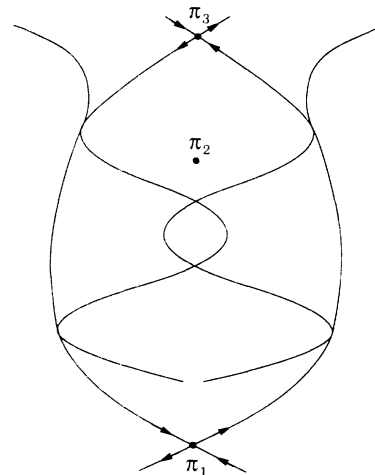


FIG. 13. Heteroclinic tangency at $V_2 = V_{h1}$.

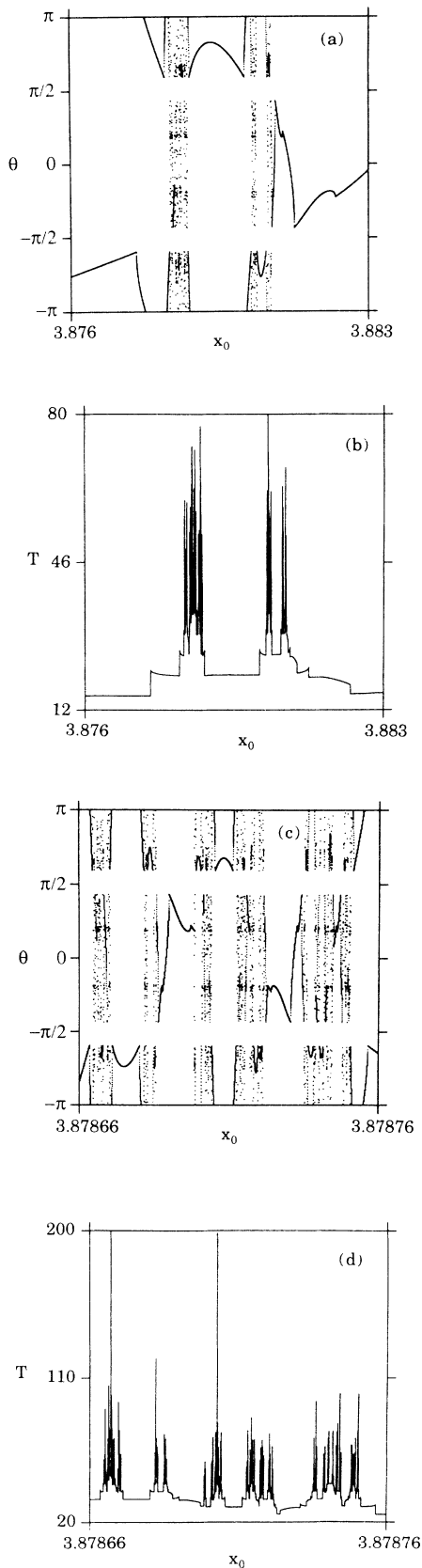


FIG. 14. (a) and (b) exit angle vs the impact parameter; (b) and (d) exit time vs the impact parameter; (c) and (d) enlargements of (a) and (d), respectively ($V_2=0.25$).

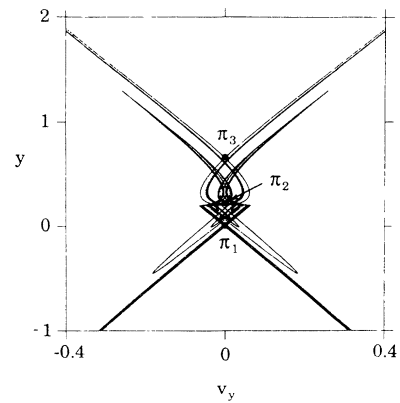


FIG. 15. The stable and unstable manifolds of π_1 and π_3 and their heteroclinic intersections ($V_2=0.25$).

are at small angles. Thus we believe that it is reasonable to conclude that there is an interval $V'_- < V_2 < V'_+$ in which the invariant set is hyperbolic. This interval exists within the interval $V_- < V_2 < V_+$. The dynamics cannot be hyperbolic in the full interval, $V_- < V_2 < V_+$, because there must be an infinite number of saddle-center bifurcations in the neighborhood of any stable-unstable manifold tangency¹¹ [in particular, at $V_2=V_-$ and $V_2=V_+$, see

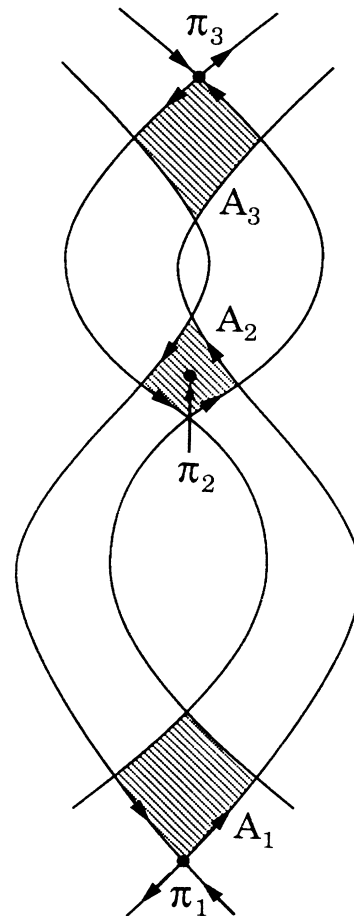


FIG. 16. The stable and unstable manifolds of π_1 and π_3 for $V_- < V_2 < V_+$.

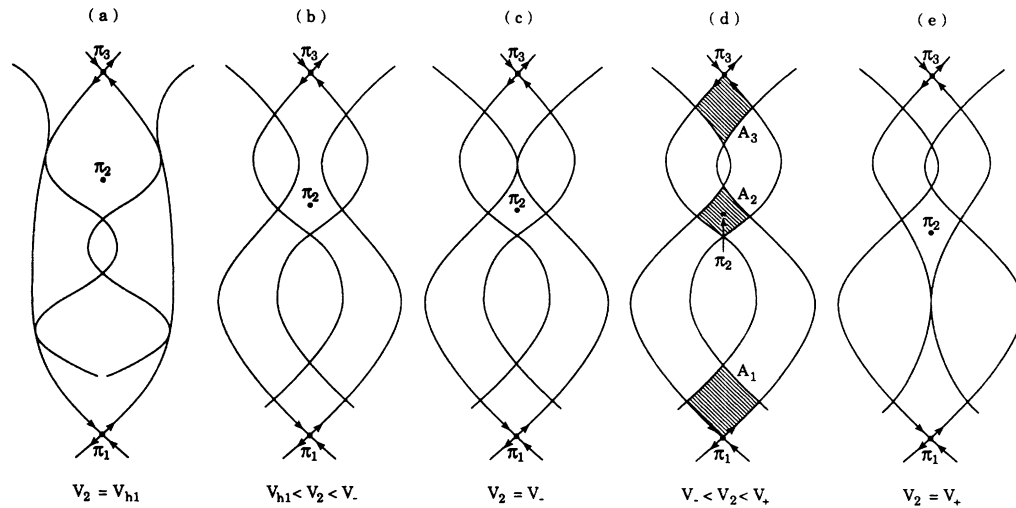


FIG. 17. Evolution patterns of the stable and unstable manifolds of π_1 and π_3 for five cases: (a) $V_2 = V_{h1}$, (b) $V_{h1} < V_2 < V_-$, (c) $V_2 = V_-$, (d) $V_- < V_2 < V_+$, and (e) $V_2 = V_+$.

Figs. 17(c) and 17(e)].

For other parameter values corresponding to potentials with hill radii relatively small compared to the distance between the hills, the situation shown in Fig. 16 can be extended up to the point where the height of the middle potential hill V_2 equals the particle energy E_p [i.e., there is no value $V_+ < E_p$ such that Fig. 17(e) applies]. For this case, we will show that an interesting bifurcation occurs as V_2 increases through E_p (see next subsection). For the remainder of this subsection we discuss the dynamics associated with Fig. 16.

Consider the three hatched diamond-shaped areas in Fig. 16 which we have denoted A_1 , A_2 , and A_3 and which are situated around the saddle orbits π_1 , π_2 , and π_3 . Figure 18 shows the images of A_1 , A_2 , and A_3 under the Poincaré map P . The structure illustrated in Figs. 16

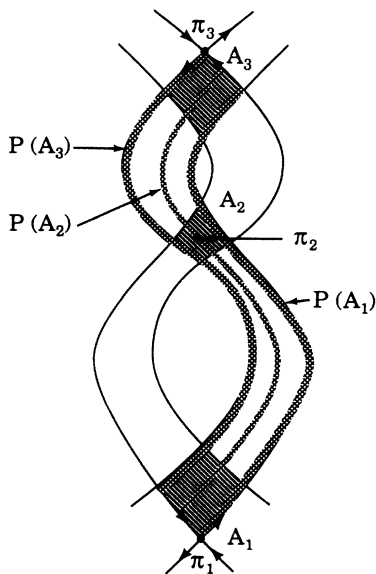


FIG. 18. The images of the three areas A_1 , A_2 , and A_3 shown in Fig. 16 under the Poincaré map P .

and 18 may be analyzed in the same manner as the classical Smale horseshoe example. To see more clearly the analogy with the Smale horseshoe, we deform the picture in Fig. 16 to obtain the topologically equivalent diagram shown in Fig. 19. The rectangle shown in Fig. 19 maps into the hatched S-shaped region which contains A_1 , A_2 , and A_3 . From the Smale horseshoe theory we know that the invariant set which contains all the orbits that stay in the original rectangle is a Cantor set and is completely contained in the three cross-hatched areas A_1 , A_2 , and A_3 . In addition, we can introduce a symbolic dynamics to describe all the orbits in the invariant set in the following way: for an orbit which travels between the three cross-hatched areas we can assign a bi-infinite symbol sequence which specifies the order in which the three cross-hatched areas are visited: $W = \dots s_{-2}s_{-1}s_0s_1s_2\dots$, where $s_j = 1, 2, \text{ or } 3$ corresponds to $A_1, A_2, \text{ or } A_3$, respectively, and $j = \dots, -2, -1, 0, 1, 2, \dots$. For a particle traveling through A_i , the corresponding leg of the trajectory in the physical space lies in the vicinity of the periodic orbit π_i (cf. Fig. 1). Thus all the bounded orbits can be coded by the three periodic orbits π_1 , π_2 , and π_3 , and the dynamics on the invariant set is organized with respect to the three periodic orbits. Given any word W ,

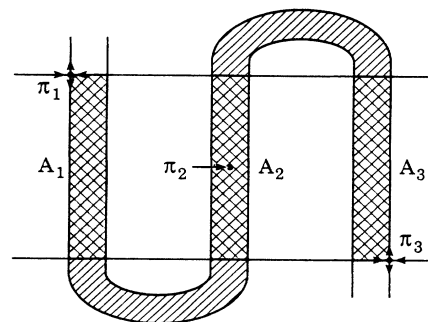


FIG. 19. The Smale horseshoe-type map obtained by deforming topologically the configuration shown in Fig. 16.

if we stipulate the direction of motion along any one orbit leg (corresponding to some s_j), then W specifies the orbit uniquely. (For example, for a chosen j value $j=J$, we might have $s_j=1$. In that case we would specify whether $s_j=1$ corresponds to an orbit leg traveling close to π_1 in the direction from hill 1 to hill 3, or, to an orbit leg traveling in the direction from hill 3 to hill 1.) This one-time specification of the orbit direction is necessary to remove the ambiguity which occurs due to the fact that the word W is, by symmetry, also the word for the orbit with $x(t)$ and $v_x(t)$ replaced by $-x(t)$ and $-v_x(t)$. If the symbol sequence is periodic then the corresponding orbit is also periodic; otherwise the corresponding orbit is aperiodic. In fact, there are a countably infinite number of periodic orbits and an uncountably infinite number of aperiodic orbits.

C. Further evolution of the system

Now let us increase V_2 beyond the value corresponding to the picture shown in Fig. 16. As mentioned in the previous subsection there are two situations.

Case (1). For relatively large hill radii (e.g., the parameter values specified at the beginning of this section) the hyperbolic range is below $V_2=E_p$, i.e., $V'_- < V_2 < V'_+$ $< E_p$.

Case (2). For relatively small hill radii compared to the separation of the hills the dynamics remains hyperbolic as $V_2 \rightarrow E_p$.

In each of these cases the evolution of the system with increasing V_2 follows a distinct route.

Case (1). In this case, as V_2 increases from the value corresponding to Fig. 16, we come to a point, $V_2=V_{h2}$ ($V_{h2} \approx 0.5$), at which another heteroclinic tangency takes place. This tangency is similar in nature to the one occurring at $V_2=V_{h1}$ (cf. Fig. 13 and Sec. III B) and is schematically illustrated in Fig. 20. Essentially as V_2 increases through V_{h2} , the interaction between the saddles π_1 and π_3 comes to an end. Above V_{h2} the stable and unstable manifolds of π_3 pull out of the tangle and leave the stable and unstable manifolds of π_1 still entangled in a complex manner. This is shown schematically in Fig. 21

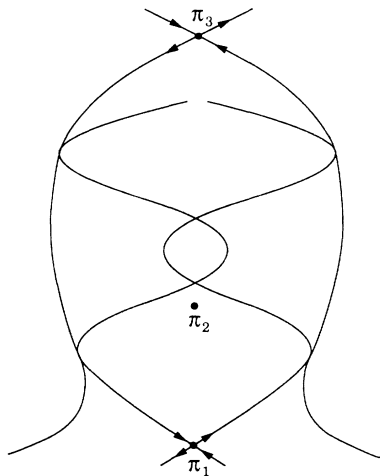


FIG. 20. Heteroclinic tangency at $V_2=V_{h2}$.

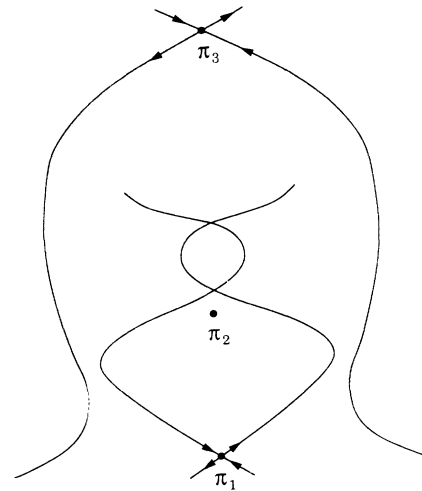


FIG. 21. The stable and unstable manifolds of π_1 and π_3 for $V_2 > V_{h2}$.

for V_2 slightly larger than V_{h2} . Physically, the heteroclinic tangency at $V_2=V_{h2}$ has strong implications for the observable scattering functions. Suppose that $V_2 > V_{h2}$ and that we send in particles from above as we did before for $V_2 < V_{h2}$. In this case, we find that the scattering is regular and governed by the saddle π_3 and its associated invariant manifolds. This is because the chaotic set is completely enclosed within the region bounded by the downward-going branches of the stable and unstable manifolds of π_3 (see Fig. 21). Hence the chaotic set is not accessible to orbits coming from above. However, we can still observe chaotic scattering if we send particles upward from below the potential. In that case, for those particles exiting downward there is chaotic behavior in the scattering functions. The situation is very similar to the one observed before the first heteroclinic tangency at $V_2=V_{h1}$ [cf. Fig. 9(c)]. In that case, the chaotic scattering is manifested by particles being sent from *above* the potential and exiting upward (cf. Figs. 12). In the current situation the roles of “above” and “below,” “upward” and “downward” are reversed, and the roles of π_1 and π_3 are also reversed. Further aspects of the system evolution and the associated symbolic dynamics for the potential system specified at the beginning of this section are discussed in Appendices B and C.

Case (2). When the hill radii are relatively small, the picture shown in Fig. 16 and the associated symbolic dynamics remain a valid description of the scattering process throughout the interval $V_- < V_2 < E_p$. At $V_2=E_p$, a new type of bifurcation which vastly alters the chaotic set takes place. We call this bifurcation a “massive bifurcation.” The phenomenology of the massive bifurcation is the following. In the physical space, as $V_2 \rightarrow E_p$ from below, the midpoint of the periodic orbit π_3 approaches the center of hill 2 ($x=0$ and $y=y_2$) [Figs. 22(a) and 22(b)] and the period of π_3 approaches infinity. At the same time, in the surface of section, as $V_2 \rightarrow E_p$ from below, the area of A_3 goes to zero. As V_2 goes through the bifurcation value E_p , the single periodic orbit π_3 bifurcates into two distinct periodic orbits of finite period.

One of these two bifurcated orbits travels back and forth between hill 3 and hill 2, while the other travels back and forth between hill 1 and 2 [Fig. 22(c)]. Due to the reflection symmetry in the potential, these two orbits are mirror images of each other. In what follows we collectively denote these two orbits as π_3 . Figures 22 summarize the evolution of the orbit π_3 for $V_2 < E_p$, $V_2 = E_p$, and $V_2 > E_p$. For $V_2 > E_p$ we can again construct a full shift of three symbols to characterize the dynamics. Specifically, for a bounded orbit, we assign a letter i to the leg of its trajectory which lies in the vicinity of the periodic orbit π_i , and a corresponding bi-infinite symbol sequence, $W = \dots s_{-2}s_{-1}s_0s_1s_2 \dots$, where $s_j = 1, 2$, or 3 for $j = \dots, -2, -1, 0, 1, 2, \dots$. (Note here that $s_j = 3$ corresponds either to an orbit leg that goes from hill 1 to hill 2 and back to hill 1 or from hill 3 to hill 2 and back to hill 3). Again the following one-time stipulation makes the correspondence between W and an orbit unique: For any symbol s_j of W we stipulate either the direction of the motion along the leg, if $s_j = 1$ or 2 , or, if $s_j = 3$, we stipulate to which of the two components of π_3 (the one in $x > 0$ or the one in $x < 0$) the leg corresponds. Finally, we note that the hatched areas of A_1 and A_2 in Fig. 16 remain finite throughout the bifurcation. Therefore, for those bounded orbits described completely by π_1 and π_2 , nothing changes at the bifurcation. This implies that we have a full shift on two symbols even at $V_2 = E_p$.

From the above discussion we conclude that, when the massive bifurcation occurs, an infinite number of bounded orbits are destroyed and a new infinite class of bounded orbits is created. The dynamics before and after the bifurcation can be characterized by a full shift on three symbols. In a forthcoming paper we plan to present

more detailed analysis on this bifurcation and discuss its consequences.¹²

IV. CONCLUSIONS

The three main general contributions of this paper are

A. the demonstration of how chaotic scattering can occur and evolve as a result of an initial saddle-center bifurcation; B. the observation that clear, sudden qualitative changes in the scattering function (θ versus x_0) occur as a result of the onset of heteroclinic intersections on the surface of section; and C. the observation of a new type of bifurcation called a massive bifurcation which leads to a radical change in the dynamics of the hyperbolic chaotic set but preserves its symbolic dynamics (Sec. III C).

We have established the above results via a detailed study of a specific potential. Our study has also shown the following.

1. The regular scattering process is characterized by features observed in both the scattering functions and particle decay plots. These features can be fully understood in terms of the finite number of unstable periodic orbits (e.g., the single orbit π_1 for the case in Sec. II) and their stable and unstable manifolds.

2. A transition from regular to chaotic scattering can occur via a saddle-center bifurcation which results in the creation of a pair of periodic orbits. One of them is a regular saddle and the other is a stable center surrounded by an island which contains periodic, quasiperiodic, and chaotic orbits.

3. The center undergoes period-doubling bifurcation and becomes an unstable twisted saddle. It appears that this period-doubling process carries on *ad infinitum* converting the center into a chaotic set containing an infinite number of periodic orbits.

4. After the saddle-center bifurcation, chaotic scattering behavior in the scattering function is observed. The corresponding chaotic set is generated by the homoclinic intersection of the stable and unstable manifolds of the saddle created at the saddle-center bifurcation (orbit π_3). Note that in this case the chaos can only be manifested by particles exiting upward when incident from above.

5. At $V_2 = V_{h1}$ the first heteroclinic tangency occurs. Above $V_2 = V_{h1}$ the scattering process suddenly undergoes a qualitative change by exhibiting chaotic behavior for particles both exiting upward and downward. This change is induced by the heteroclinic intersections between the two sets of stable and unstable manifolds of π_1 and π_3 .

6. Fully developed chaos involving bounded orbits traveling between π_1 , π_2 , and π_3 in arbitrary order is reached when the configuration shown in Fig. 16 is realized. Based on this configuration we can construct a horseshoe-type map. The resulting chaotic set is completely hyperbolic and is characterized by a full shift of three symbols.

7. Increasing V_2 further from the value corresponding to Fig. 16, the system can evolve following either one of the two distinct routes depending on the configuration of the potential. Along the first route, the two sets of stable

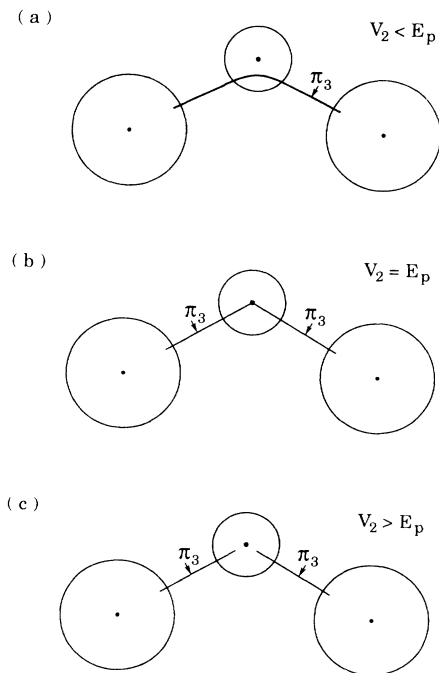


FIG. 22. The periodic orbit π_3 for three cases: (a) $V_2 < E_p$, (b) $V_2 = E_p$, and (c) $V_2 > E_p$.

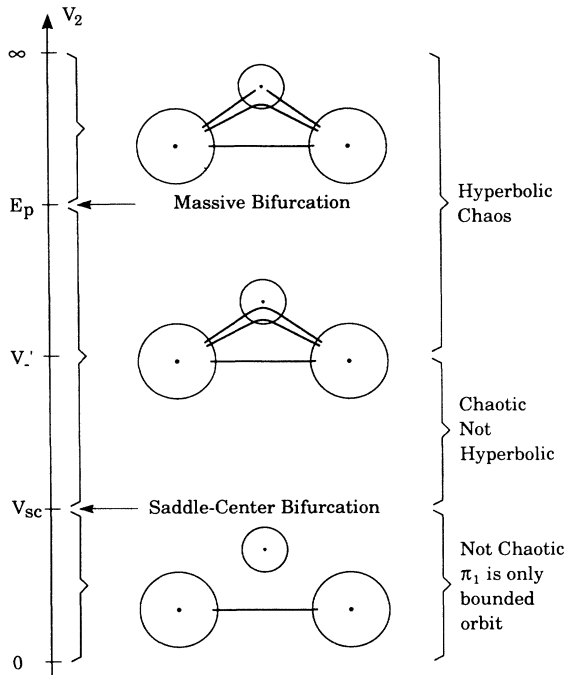


FIG. 23. Summary of the major phenomenological changes in the dynamics as V_2 is increased from zero for the case where the hill radii are relatively small compared to the distance between the hills.

and unstable manifolds of π_1 and π_3 detach from each other and the scattering process experiences another qualitative change, in which, if we send in particles from above, no chaotic scattering can be observed; while if we send in particles from below, such particles can exhibit chaotic behavior. Along the second route, the system undergoes a massive bifurcation in which an infinite number of bounded orbits are destroyed and replaced by a new infinite class of bounded orbits, and the symbolic dynamics remains the same.

Figure 23 pictorially summarizes the major phenomenological changes in the dynamics as V_2 is increased from zero for the case where the hill radii are relatively small compared to the distance between the hills (see Sec. III C).

ACKNOWLEDGMENTS

We thank Qi Chen for useful comments and discussions. This work was supported by the U.S. Department of Energy (Basic Energy Science) and the Office of Naval research (Physics Division).

APPENDIX A: DISCUSSION OF EQ. (4)

To understand the exponent $\mu = \ln(\lambda_p)/T_p$ in terms of the properties of π_1 , we need to analyze our second numerical experiment discussed in Sec. II on the particle decay process. As we have mentioned before, the closer an initial condition is to the stable manifold, the longer it takes to exit the potential region. Here “longer” also means that the particle bounces more times between the two hills. In the process of moving an initial condition

closer and closer to the stable manifold, the corresponding trajectory experiences tangencies with the boundaries, $(x-x_i)^2 + (y-y_i)^2 = a_i^2$, of either of the two hills ($i=1,3$) alternatively. At such a tangency the time T jumps discontinuously. These jumps are clearly seen in the exit time plots Figs. 4(b) and 4(d). Let $L(I_n)$ denote the length of the interval I_n of initial conditions corresponding to orbits which bounce n times between the two hills, and let $L(I_{n+1})$ denote the length of the interval I_{n+1} of initial conditions corresponding to orbits which bounce $n+1$ times between the two hills. For $n \gg 1$ these lengths scale as

$$L(I_{n+1})/L(I_n) \sim 1/\lambda_1, \quad (\text{A1})$$

where λ_1 is the eigenvalue at π_1 . Since the initial conditions are spaced uniformly, the number of particles in the subinterval I_n scales with λ_1 as $1/\lambda_1^n$.

Equation (A1) can be understood in the following way. Consider the point q of the upward branch of the unstable manifold shown in Fig. 6 and its consecutive images under the inversed Poincaré map P^{-1} [change the particle velocity from v to $-v$, then the surface of section points of the resulting trajectory are $P^{-1}(q)$, $P^{-2}(q)$, ..., etc]. The point q in Fig. 6 has been so chosen that the forward trajectory from q experiences a tangency with either of the two hills depending on the sign of v_x and then leaves the potential region. The forward trajectories going through points in the interval from $P^{-1}(q)$ to q on the unstable manifold bounce once from either hill 1 or hill 3 and then leave the potential region without ever returning to it. The forward trajectories going through points in the interval from $P^{-2}(q)$ to $P^{-1}(q)$ experience two bounces before heading off to infinity. In general, the forward trajectories going through the interval from $P^{-n}(q)$ to $P^{-n+1}(q)$ bounce n times between the two hills. If we use D_n to denote the length of the interval from $P^{-n}(q)$ to $P^{-n+1}(q)$ and D_{n+1} to denote the length of the interval from $P^{-(n+1)}(q)$ to $P^{-n}(q)$, then they scale as

$$D_{n+1}/D_n \sim 1/\lambda_1. \quad (\text{A2})$$

The above argument and Eq. (A2) also apply to the downward branch of the unstable manifold. Our third experiment discussed in Sec. II shows that a segment on the initial condition line $y=6$ containing the intersection of the stable manifold with that line crosses the surface of section (cf. Fig. 7). Forward iterations of the image of the line segment under P move it along the stable manifold toward π_1 and closer and closer to the unstable manifold. For large enough iterations, the motion of the image of the initial segment is approximately aligned along the unstable manifold of π_1 . Thus Eq. (A1) follows from Eq. (A2).

Note that for $n \gg 1$ in Eq. (A1), the following relation holds: the length of an orbit bouncing $n+1$ times is approximately equal to the length of an orbit bouncing n times plus one-half the period of π_1 . Let T_π denote the period of the periodic orbit π_1 . Suppose now that at time T all particles with initial conditions in I_i where $i \leq n-1$ have already left the potential, then at time $T + T_\pi/2$ all

those particles in I_n will also have left the potential. Thus we can identify λ_p and T_p defined in Fig. 5(b) with λ_1 and $T_\pi/2$. Hence we have

$$\lambda_p = \lambda_1 \quad (\text{A3})$$

and

$$T_p = T_\pi/2. \quad (\text{A4})$$

If we take the logarithm of the number of particles $N(T)$ still left in the region at time T and plot it against T , we will get vertically equally spaced steps, and the width and height of these steps are $T_p = T_\pi/2$ and $\ln \lambda_p = \ln \lambda_1$ as shown in Fig. 5(b).

APPENDIX B: SYMBOLIC DYNAMICS OF TWO SYMBOLS AND THEIR ROLE IN THE SYSTEM EVOLUTION

In this appendix we extend further our discussion on the configuration shown in Fig. 16. For the purpose of the following discussion it is useful to consider a subset of the orbits previously defined on the three symbols A_1 , A_2 , and A_3 . Specifically, we note that to any sequence of the two symbols A_1 and A_3 there is a corresponding orbit for Fig. 16 which visits the regions A_1 and A_3 in the appropriate order.

In Fig. 24 we draw a more detailed picture of the configuration shown in Fig. 16, emphasizing the structures of the stable and unstable manifolds near the two saddles π_1 and π_3 . In Figs. 16 and 24, the vertices of the diamond-shaped region A_1 are C_1^1 , π_1 , W_1^- , and W_1^+ , and the vertices of A_3 are C_3^1 , π_3 , W_3^- , and W_3^+ . Consider the hatched diamond-shaped area in Fig. 24 denoted by $A_1^3 \subset A_1$. As can be seen in the figure, this area is defined by the four points C_1^3 , π_1 , $P(W_1^-)$, and $P^{-1}(W_1^+)$ and the stable and unstable manifolds of π_1 and π_3 con-

necting these points, where $P(W_1^-)$ is the forward iteration of the heteroclinic point W_1^- under the Poincaré map P , and $P^{-1}(W_1^+)$ is the backward iteration of the heteroclinic point W_1^+ under P . Let us also consider the hatched diamond-shaped area $A_3^3 \subset A_3$. This area is defined by the four points C_3^3 , π_3 , $P(W_3^-)$, and $P^{-1}(W_3^+)$ and the stable and unstable manifolds connecting these points, where $P(W_3^-)$ is the forward iteration of the heteroclinic point W_3^- under the Poincaré map P , and $P^{-1}(W_3^+)$ is the backward iteration of the heteroclinic point W_3^+ , under P . It is not hard to argue that a horseshoe-type dynamics is applicable to these two hatched areas if we consider the third iteration of the Poincaré map P^3 instead of P . Then for any bi-infinite sequence made of the two symbols A_1^3 and A_3^3 , there will be an orbit traveling between the two areas in the same order under the map P^3 . In Fig. 16 an orbit starting from the surface of section only needs one bounce from either hill 1 or hill 3 to hop from one of the hatches areas, A_1 or A_3 , to the other; while an orbit with initial condition in one of the smaller hatched areas, A_1^3 and A_3^3 shown in Fig. 24, needs to bounce three times between hills 1 and 3 to go from one to the hatched areas, A_1^3 or A_3^3 , to the other. This interpretation agrees with our intuition that a particle with smaller initial y velocity v_y takes longer time to reach the same height vertically.

Generally, we can imagine even smaller diamond-shaped areas A_1^{2n+1} and A_3^{2n+1} . A_1^{2n+1} is defined by the four points C_1^{2n+1} , π_1 , $P^n(W_1^-)$, and $P^{-n}(W_1^+)$ and the stable and unstable manifolds of π_1 and π_3 connecting these points; A_3^{2n+1} is defined by the four points C_3^{2n+1} , π_3 , $P^n(W_3^-)$, and $P^{-n}(W_3^+)$ and the stable and unstable manifolds of π_1 and π_3 connecting these points. For the two areas, A_1^{2n+1} and A_3^{2n+1} , an associated symbolic dynamics is also applicable if we consider the Poincaré map P^{2n+1} , where n is any positive integer. Note that for $n \gg 1$ the area of A_1^{2n+1} and the area of A_1^{2n-1} scale as

$$\mathcal{A}(A_1^{2n+1})/\mathcal{A}(A_1^{2n-1}) \sim 1/\lambda_1^2, \quad (\text{B1})$$

where λ_1 is the unstable eigenvalue of P at π_1 , and the area of A_3^{2n+1} and the area of A_3^{2n-1} scale as

$$\mathcal{A}(A_3^{2n+1})/\mathcal{A}(A_3^{2n-1}) \sim 1/\lambda_3^2, \quad (\text{B2})$$

where λ_3 is the unstable eigenvalue of P at π_3 .

Thus we find the following sequence of events leading to the situation shown in Fig. 16. At $V_2 = V_{h1}$ (cf. Fig. 13), all the diamond-shaped areas A_1 , $A_1^3, \dots, A_1^{2n+1}, \dots$ are formed close to the saddle π_1 , but none of the A_3^{2n+1} are formed. When V_2 slightly exceeds V_{h1} , only the small, higher n diamond-shaped areas A_3^{2n+1} lying close to the saddle π_3 have been formed. As V_2 increases, successively more, lower n areas A_3^{2n+1} form. Figure 25 shows the situation where the A_3^5, A_3^7, \dots diamonds have come into existence, while A_3 and A_3^3 have not yet formed. Increasing V_2 above the value corresponding to Fig. 25, we see that the pair of cross-hatched areas, one between W_3^- and $P(W_3^-)$ and the other between W_3^+ and $P^{-1}(W_3^+)$ move in toward each other and then intersect each other. This intersection implies

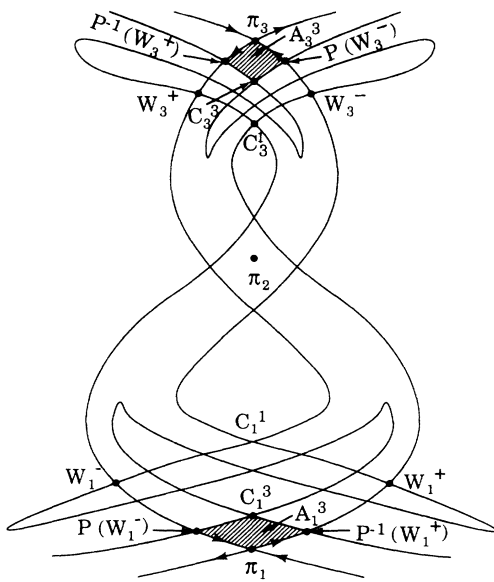


FIG. 24. More detailed structure of the stable and unstable manifolds of π_1 and π_3 for the case shown in Fig. 16.

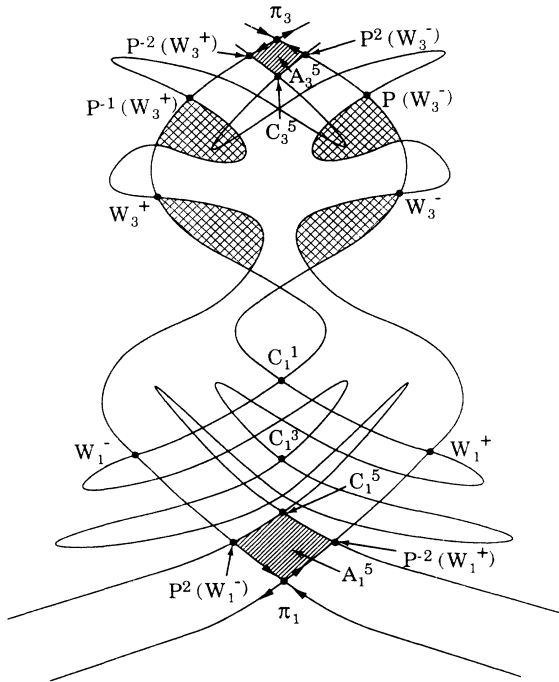


FIG. 25. The diamond-forming process in the vicinity of π_3 .

the formation of A_3^3 . If we increase V_2 further, the other pair of the cross-hatched areas will also come in toward each other and make intersections. In this case, A_3 has formed, and we reach the configuration shown in Fig. 16.

We note that the process from Fig. 16 to the heteroclinic tangency ($V_2 = V_{h_2}$) shown in Fig. 20 following the evolution route discussed in Case (1) of Sec. III C is similar to that described above. In particular, to utilize that discussion consider the reversed evolution from Fig. 20 to Fig. 16. As we decrease the value V_2 from V_{h_2} to that corresponding to Fig. 16, we observe a forming process of increasing V_2 , except that the roles of the two saddles π_1 and π_3 are switched. Thus for $V_2 > V_+$ we lose the largest diamond-shaped area situated near π_1 and its associated symbolic dynamics of three symbols. Increasing V_2 further the smaller diamond-shaped areas and their corresponding symbolic dynamics of two symbols disappear in ascending order.

APPENDIX C: ANOTHER PARAMETER VARIATION

Now we examine how the system evolution we have observed in Sec. III for increasing V_2 is altered if other

system parameters are changed. More specifically, we fix the inner edges of hills 1 and 3 (i.e., the points $x = x_1 - a_1$ and $x = x_3 + a_3$) and let their radii $a_1 = a_2 = R$ vary. We then examine the sequence of events for fixed R as V_2 is increased, and we ask how this sequence is changed if we change R . In the case $R = \infty$, we obtain a system consisting of one potential hill (hill 2) sandwiched between two planar potentials. No chaos can occur in such a system because the only orbit which interacts with hill 2 forever is the one bouncing between the planes (along the x axis) and passing directly through the center of the hill 2. (Here we assumed $V_2 < E_p$ where E_p is the particle energy. For $V_2 > E_p$ there are two periodic orbits, one in $x > 0$ and one in $x < 0$.) Since the limiting system described above can be gradually reached from the one shown in Fig. 1, we can ask how the chaos created in Sec. III disappears. For fixed $a_1 = a_3 = R \neq \infty$, we find that the saddle-center bifurcation always occurs as V_2 is increased. This implies that chaotic scattering can be observed. However, the scenario of the system evolution we have established in Sec. III undergoes alterations if we examine the system behavior with increasing V_2 for different values of R . Imagine a particle lying close to the saddle π_1 , and assume it has a small but positive initial y velocity. Then the larger is R , the more bounces are needed for the particles to reach a given vertical height, say, the place where the saddle π_3 is located. The reason is that the particle acquires only a small upward velocity from each deflection from hills 1 or 3 because their surfaces are almost flat. This implies that we can find a value of R , say R_1 , such that, for any fixed $R > R_1$, we no longer observe the horseshoe-type map corresponding to P (i.e., Fig. 16) with increasing V_2 . We can further find another value of R , say $R_3 > R_1$, such that for any fixed $R > R_3$, the horseshoe-type map corresponding to P^3 vanishes from the sequence of events of the system evolution with increasing V_2 . In general, we can find R_{2n+1} so that, for any fixed $R > R_{2n+1}$, the horseshoe-type map corresponding to P^{2n+1} disappears from the pattern of the system evolution with increasing V_2 . Eventually, the limiting case of $R = \infty$ is reached, where no saddle-center bifurcation (therefore no chaotic scattering) can occur. We have numerically examined this scenario and verified it up to R_3 . (In particular, for the numerical system defined in Sec. III, $a_1 = a_3 = R = 12$ is in the interval $[R_1, R_3]$.)

*Present address: Center for Complex Systems and Department of Mathematics, Florida Atlantic University, Boca Raton, FL 33431.

¹J. M. Petit and M. Hénon, *Icarus* **66**, 536 (1986).

²D. W. Noid, S. Gray, and S. A. Rice, *J. Chem. Phys.* **84**, 2649 (1986).

³B. Eckhardt and H. Aref, *Philos. Trans. R. Soc. London, Ser. A* **326**, 655 (1988); B. Eckhardt, *Europhys. Lett.* **5**, 107 (1988); S. Manakov and L. N. Schur, *Pis'ma Zh. Eksp. Teor. Fiz.* **37**, 45 (1983) [*JETP Lett.* **37**, 54 (1983)].

⁴R. C. Churchill, G. Pecelli, and D. L. Rod, in *Como Conference Proceedings on Stochastic Behavior in Classical and Quantum Hamiltonian Systems*, Vol. 93 of *Springer Lecture Notes on Physics*, edited by G. Casati and J. Ford (Springer, New York, 1979), p. 79; B. Eckhardt and C. Jung, *J. Phys. A* **19**, L829 (1986); M. Hénon, *Physica D* **33**, 132 (1989); C. Jung and H. J. Scholz, *ibid.* **20**, 3607 (1987); B. Eckhardt, *Physica D* **33**, 89 (1988); R. Blümel and U. Smilansky, *Phys. Rev. Lett.* **60**, 477 (1988); P. Gaspard and S. Rice, *J. Chem. Phys.* **90**, 2225 (1988); Z. Kovács and T. Tél, *Phys. Rev. Lett.* **64**,

- 1617 (1990); T. Tél, *J. Phys. A* **22**, L691 (1989).
- ⁵G. Trolldenier and U. Smilansky, in *Chaos and Quantum Physics*, Proceedings of the Les Houches Summer School, Session LII, 1989, edited by M.-J. Giannoni, A. Voros, and J. Zinn-Justin (Elsevier, Amsterdam, in press).
- ⁶S. Bleher, E. Ott, and C. Grebogi, *Phys. Rev. Lett.* **63**, 919 (1989); S. Bleher, C. Grebogi, and E. Ott, *Physica D* (to be published).
- ⁷G. Hsu, E. Ott, and C. Grebogi, *Phys. Lett. A* **127**, 199 (1988).
- ⁸C. Robinson, *Am. J. Math.* **92**, 562 (1970).
- ⁹J. Meiss and E. Ott, *Phys. Rev. Lett.* **55**, 2741 (1985), and references therein.
- ¹⁰K. Alligood, E. Yorke, and J. A. Yorke, *Physica D* **28**, 197 (1987).
- ¹¹S. Newhouse, *Topology* **13**, 9 (1974).
- ¹²M. Ding, C. Grebogi, E. Ott, and J. A. Yorke (unpublished).